Clim Dyn (2010) 35:807–826
DOI 10.1007/s00382-009-0595-7

Further analysis of singular vector and ENSO predictability in the Lamont model—Part I: singular vector and the control factors

Yanjie Cheng · Youmin Tang · Xiaobing Zhou · Peter Jackson · Dake Chen

Received: 4 February 2009 / Accepted: 11 May 2009 / Published online: 27 May 2009
© Springer-Verlag 2009

Abstract In this study, singular vector analysis was performed for the period from 1856 to 2003 using the latest Zebiak–Cane model version LDEO5. The singular vector, representing the optimal growth pattern of initial perturbations/errors, was obtained by perturbing the constructed tangent linear model of the Zebiak–Cane model. Variations in the singular vector and singular value, as a function of initial time, season, ENSO states, and optimal period, were investigated. Emphasis was placed on exploring relative roles of linear and nonlinear processes in the optimal perturbation growth of ENSO, and deriving statistically robust conclusions using long-term singular vector analysis. It was found that the first singular vector is dominated by a west–east dipole spanning most of the equatorial Pacific, with one center located in the east and the other in the central Pacific. Singular vectors are less sensitive to initial conditions, i.e., independence of seasons and decades; while singular values exhibit a strong sensitivity to initial conditions. The dynamical diagnosis shows that the total linear and nonlinear heating terms play opposite roles in controlling the optimal perturbation growth, and that the linear optimal perturbation is more than twice as large as the nonlinear one. The total linear heating causes a warming effect and controls two positive perturbation growth regions: one in the central Pacific and the other in the eastern Pacific; whereas the total linearized nonlinear advection brings a cooling effect controlling the negative perturbation growth in the central Pacific.

Keywords ENSO · Predictability · Singular vector analysis

Y. Cheng · Y. Tang (✉) · X. Zhou · P. Jackson
Environmental Science and Engineering, University of Northern British Columbia, 3333 University Way, Prince George, BC V2N 4Z9, Canada
e-mail: ytang@unbc.ca

D. Chen
Lamont-Doherty Earth Observatory of Columbia University, Palisades, NY 10964, USA

D. Chen
State Key Laboratory of Satellite Ocean Environment Dynamics, Hangzhou, China

Present Address:
X. Zhou
Centre for Australian Weather and Climate Research (CAWCR), Bureau of Meteorology, 700 Collins St, Melbourne, VIC 3001, Australia

1 Introduction

ENSO is the strongest interannual variability in the global climate system. It happens in the tropical Pacific Ocean with a period of 2–7 years and has world-wide climatic, ecological, and social impacts. Significant progress has been made in understanding and predicting ENSO over the past few decades. At present, there are many ENSO prediction models with differing levels of complexity, including intermediate coupled models, hybrid coupled models and fully coupled general circulation models (GCM). When measured by the anomaly correlation between the predicted and observed sea surface temperature anomalies (SSTA) in the eastern Pacific, these models generally have prediction skills as measured by the correlation over 0.5 for lead times of 6–12 months (Latif et al. 1998; Kirtman et al. 2002; Chen and Cane 2008). However, some important issues still remain unsolved such as the relationship between potential predictability and the actual prediction skill and the control factors of predictability.

Generally, there are several sources that limit ENSO predictability: uncertainty in initial conditions and model parameters; the chaotic behavior of the nonlinear dynamics of the coupled system (e.g., Jin et al. 1994; Chen et al. 2004) and the atmospheric noise and other high-frequency variations such as westerly wind bursts and the Madden–Julian oscillation (e.g., Penland and Sardeshmukh 1995; Kleeman and Moore 1997; Vecchi and Harrison 2003; Moore et al. 2006; Gebbie et al. 2007). Some studies suggested that the model-based prediction of ENSO depends more on the initial conditions than on unpredictable atmospheric noise (i.e., Tang and Hsieh 2003; Chen et al. 2004).

A widely used strategy in studying initial perturbation growth is through singular vector (SV) analysis, a method to describe optimal perturbation growth. The earliest work using SV analysis to explore the growth of initial errors was documented in Lorenz (1965). In recent years, a number of models have been used to explore optimal perturbation growth of ENSO predictions using SV analysis. Chen et al. (1997) used the Battisti (1988) version of Zebiak–Cane (ZC) model to calculate the SV and found that the optimal perturbation pattern consists of an east-west dipole in the entire tropical Pacific basin superimposed on a north–south dipole in the eastern tropical Pacific. Xue et al. (1997a, b) constructed a tangent linear model (TLM) in an EOF-reduced space for the ZC model via the Markov method. Their SV spatial distribution was similar to that of Chen et al. (1997). Fan et al. (2000), using a different intermediate complexity coupled model, found that the optimal perturbation growth depends critically on the seasonal cycle and ENSO phase as well as the prediction lead time. Tang et al. (2006) studied ENSO potential predictability using a fully coupled GCM and discussed some deficiencies in the GCM and their possible influences on SV growth. Zhou et al. (2007) explored the impact of atmospheric nonlinearity on the optimal perturbation growth by comparing SVs of two ENSO models that have the same oceanic model coupled, respectively, to a linear and a nonlinear statistical atmospheric model.

However, there are still challenging issues concerning optimal perturbation growth that warrant further investigation. First, all of the above studies focused on a period of only 20–40 years, with a rather limited number of ENSO cycles, basically precluding statistically robust conclusions. A longer-term SV analysis would result in more robust ensemble feature of SV. Second, it has been well recognized that the actual predictability of ENSO has striking decadal/interdecadal variations (e.g., Chen et al. 2004; Tang et al. 2008). One might be able to shed light on the mechanism of decadal/interdecadal variation in ENSO predictability by exploring decadal/interdecadal variation of the optimal perturbation growth by SV analysis. Obviously, the SV analysis for only a 20–40 year period, as performed previously, is unable to achieve this goal. Third, it has been of great interest to identify the sources and processes that limit the predictability of ENSO. Nonlinearity and stochastic noise are generally thought to be two most important factors limiting ENSO predictability. One effective method to explore the importance of nonlinearity in ENSO predictability might be to examine the relative roles that linear and nonlinear processes play in optimal perturbation growth, which has not been well addressed in previous studies. Finally, the relationship between optimal perturbation growth and the actual model prediction skill, i.e., between the potential predictability and actual predictability, should be examined under a framework of statistically robust analysis.

Thus, further SV analysis is required to more fully understand optimal perturbation growth and ENSO predictability. In this first part of a two paper study of ENSO predictability, the first three challenges discussed above are addressed. In part two of the study, we will focus on actual model prediction skills and their relationship to optimal perturbation growth over a long-term period, which will provide insights on mechanisms of ENSO predictability. Recently, Chen et al. (2004) used KAPLAN sea surface temperature anomaly (SSTA) reanalysis data and the ZC model (LDEO5 version) to perform a 148 year hindcast experiment for the period of 1856–2003. They successfully predicted all of the prominent El Niño events during this period at lead times of up to 2 years, with the SST being the only data used for model initialization. Tang et al. (2008) further analyzed the interdecadal variation in ENSO prediction skill from 1881 to 2000 using multiple models. These retrospective ENSO predictions allow us to achieve a robust and stable study of statistical predictability of ENSO.

In the present paper, we perform SV analysis for the ZC model version LDEO5, from 1856 to 2003 using a newly constructed TLM, then explore ENSO predictability using SV analysis. To our knowledge, this study is the first attempt to explore optimal perturbation growth of ENSO predictions by SV analysis for a period over 100 years. Emphasis will be placed on the first three aforementioned issues, in particular, investigating possible control factors and mechanisms responsible for variations in the SV. Section 2 briefly introduces the LDEO5 model, the construction of the TLM, and the SV method. Section 3 presents the optimal perturbation growth pattern and perturbation growth rate by SV analysis. In Sect. 4, the variability of SSTA is dynamically diagnosed and the dominant factors controlling the perturbation growth, i.e., nonlinear heating (NH) and linear heating (LH), are discussed, followed by a conclusion and discussion in Sect. 5.

2 Methods

2.1 ZC model LDEO5 version

The model used in this study is the Zebiak and Cane model (Zebiak and Cane 1987; hereafter ZC), which has been widely applied for ENSO simulation and prediction. LDEO5 is the latest version of ZC model (Chen et al. 2004). For long retrospective predictions, a historic SST of the past 148 years from 1856 to 2003 has been assimilated into the coupled model using a nudging scheme (Chen et al. 2004). The skillful retrospective predictions initialized by the historic SST data, as shown in Chen et al. (2004) and Tang et al. (2008), evidence the good quality of SST initial conditions. The atmosphere dynamics follows Gill (1980) using steady-state, linear shallow-water equations. The circulation is forced by a heating anomaly which depends on the SST anomaly and moisture convergence. The ocean dynamics uses the reduced-gravity model, and ocean currents were generated by spinning up the model with monthly wind. The thermodynamics describe the SST anomaly and heat flux change. The model time-step is 10 days. The spatial region is focused on the tropical Pacific Ocean (124°E–80°W; 28.75°S–28.75°N). The grid for ocean dynamics is 2° longitude × 0.5° latitude, and the grid for SST physics and the atmospheric model is 5.625° longitude × 2° latitude.

2.2 Theory of SV analysis

The evolution of a small perturbation X of the initial state vectors of a nonlinear dynamical model can be represented as:

$$\frac{\partial X}{\partial t} = LX \tag{1}$$

where L is the linearized operator of the nonlinear model. At time $t + \Delta t$, the solution to Eq. 1 is given by

$$X(t + \Delta t) = R(t, \Delta t)X(t) \tag{2}$$

R, a function of time and the lead time, is often called the propagator and represents the perturbation growth matrices. From (1) and (2),

$$R(t, \Delta t) = \exp\left(\int_t^{t+\Delta t} L dt\right) \tag{3}$$

For the whole model domain, the amplitude of perturbation growth is defined as below,

$$\begin{aligned} A =& \frac{\|X(t + \Delta t)\|}{\|X(t)\|} = \frac{\langle X(t + \Delta t), X(t + \Delta t)\rangle^{1/2}}{\langle X(t), X(t)\rangle^{1/2}} \\ =& \frac{\langle RX(t), RX(t)\rangle^{1/2}}{\langle X(t), X(t)\rangle^{1/2}} = \frac{\langle X(t), R^* RX(t)\rangle^{1/2}}{\langle X(t), X(t)\rangle^{1/2}} \end{aligned} \tag{4}$$

where $\langle\rangle$ denotes the inner product, R^* is the transpose of R. An L-square norm is used in Eq. 4. The eigenvector (E) of R^*R is the SV of R, representing the perturbation growth patterns. Thus the SV can be obtained by two methods: the empirical orthogonal function (EOF) analysis for R^*R matrix or singular value decomposition (SVD) analysis. In this study, we use the second method,

$$R = F\Lambda E^* \tag{5}$$

where Λ is a real, positive, diagonal matrix; E and F are orthonormal (unitary) matrices. The columns of E and F are SVs and final patterns (FP). From (5), we can see the relationship between the first SV mode (E_1) and the first final pattern FP mode (F_1):

$$R(t, \Delta t)E_1 = \lambda_1 F_1 \tag{6}$$

λ_1 is the largest singular value in the Λ matrix, representing the amplitude (rate) of the optimal perturbation growth (E_1).

Generally, there are two approaches for SV analysis: a direct method and an indirect method. The direct method derives the linearized operator L in (1) and its adjoint operator from the original nonlinear model, i.e., the tangent linear model (TLM) and the adjoint model (AM), both being used for calculating the derivative and gradient of model state variables. The procedure of the direct method is to run the original model, TLM, and AM simultaneously together with an SVD (Singular value decomposition) algorithm. The application of the direct method can be found in the literature (e.g., Moore and Kleeman 1996; Li et al. 2005). The indirect method uses two steps to get the propagator (R) in (2). The first step is to integrate the original model from initial time to several months later (i.e., the optimal period) and to record the final state X'_f. In the second step, small perturbations, denoted by X_i, are added in the initial field of the original model and the original model runs grid by grid. The final state, denoted by X''_f, is recorded. The perturbation growth during the optimal period, denoted by X_f, is the difference between X''_f and X'_f and the propagator R is thus $(X''_f - X'_f)X_i^{-1}$. The maximum possible perturbation growth is the first (largest) singular value of the propagator R. The initial and final patterns that accomplish this perturbation growth are the right and left singular vectors of R.

In this study, we propose a mixed algorithm for SV analysis, in which the TLM model was directly constructed from the original ZC model but only used for producing R. The advantage of this mixed algorithm is that it maintains the computational accuracy by using TLM and avoids the technical difficulty inherent in producing the AM model. In implementation, given a perturbation onto a model grid, the TLM model integrates forward once; so that the TLM model runs as many times as the number of model grids.

The initial SSTA perturbation is 0.05°C, about 1% of the original SSTA amplitude. It should be noted that the SVs are not very sensitive to the amplitude of initial perturbations when the initial perturbation varies between ±0.25°C for SSTA, ±2 m/s for zonal and meridional wind anomalies, and ±2 m for thermocline depth anomaly (H). The total perturbation growth during the optimal period (X_f) is actually a final pattern responding to the initial perturbation (X_i). The relationship between the X_f and the X_i can be described by (2), i.e.,

$$R(t, t + \Delta t)X_i = X_f \tag{7}$$

To avoid calculating the inverse matrix X_i*, the initial perturbation is fixed at 0.05°C, thus X_i is a diagonal matrix with all diagonal elements equal to 0.05°C.

$$R(t, t + \Delta t) = \frac{X_f}{0.05} \tag{8}$$

Finally, from Eq. 5, we can find the SVs, final patterns, and singular values.

3 SV analysis over 148 years

3.1 Variations of the first SV and the final pattern

First, we only consider initial uncertainties in SST. The SV analysis is performed every month at the optimal period of 6 months (i.e., 6-month lead) for 1856–2003, using the TLM and SVD method, as discussed in Sect. 2.2. In each SV analysis, the optimal perturbation growth pattern (the first singular vector, SV1), final pattern, and perturbation growth rates (singular values) are obtained. Figure 1(a, b) show the averaged SV1 and the corresponding final pattern at 6-month lead time over 148 years. As can be seen, the SV1 is dominated by a west–east dipole in the tropical Pacific Ocean: one center located south of the equator in the eastern tropical Pacific Ocean and the other located in the central Pacific Ocean near 150°W (Fig. 1a). Such a dipole structure favorable for the perturbation growth is probably inherent in ENSO dynamics. For example, the zonal SSTA gradient at the equatorial eastern Pacific weakens local upwelling and intensifies the warm Kelvin waves propagating eastward according to the delayed oscillator theory (Suarez and Schopf 1988). The warm eastward propagating Kelvin waves bring warm waters to the eastern Pacific Ocean and further intensify the anomalies, finally leading to an El Niño-like pattern as shown in Fig. 1b. Figure 1a, b are similar to that in the SV1 and FP of the Battisti coupled atmosphere–ocean model (Chen et al. 1997) and an older version of the ZC model (Xue et al. 1997a).

In a coupled ocean–atmosphere model, initial uncertainties may come from the atmosphere as well. To examine the sensitivity of the SV1 and the final pattern to uncertainties in the atmosphere, we repeated the above SV analysis but included perturbations on the initial conditions of both the SSTA and anomalous wind (zonal wind U and

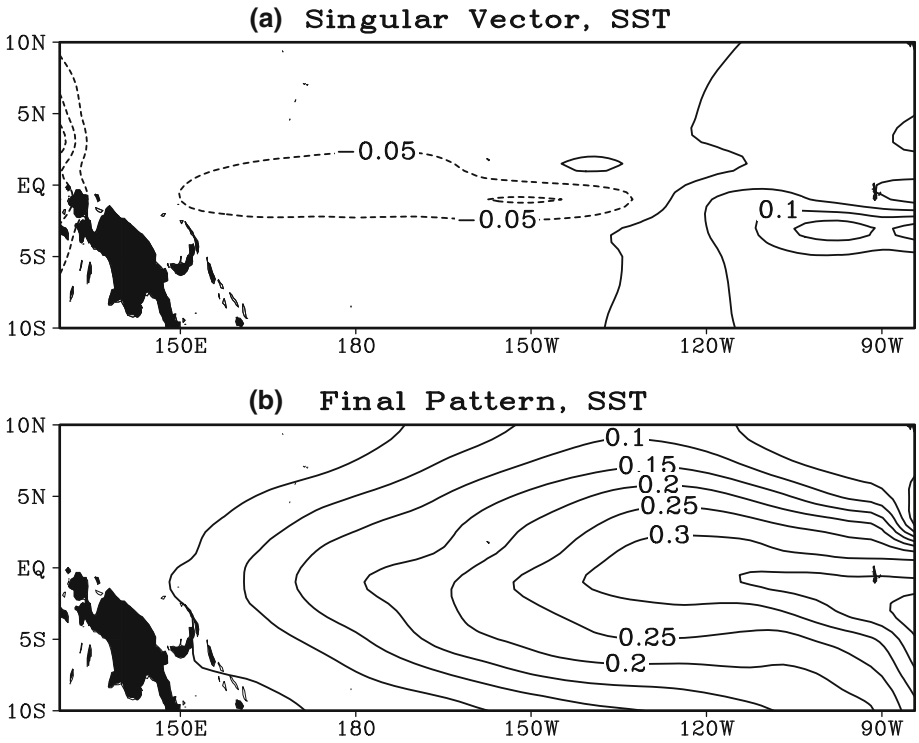

Fig. 1 The first singular vector and the first final pattern of SSTA averaged in the 148 years. **a** The first singular vector of SSTA. **b** The first final pattern of SSTA. (SV1 & FP explain 32% of the variance of R in the SVD analysis using Eq. 5) (Unit: °C)

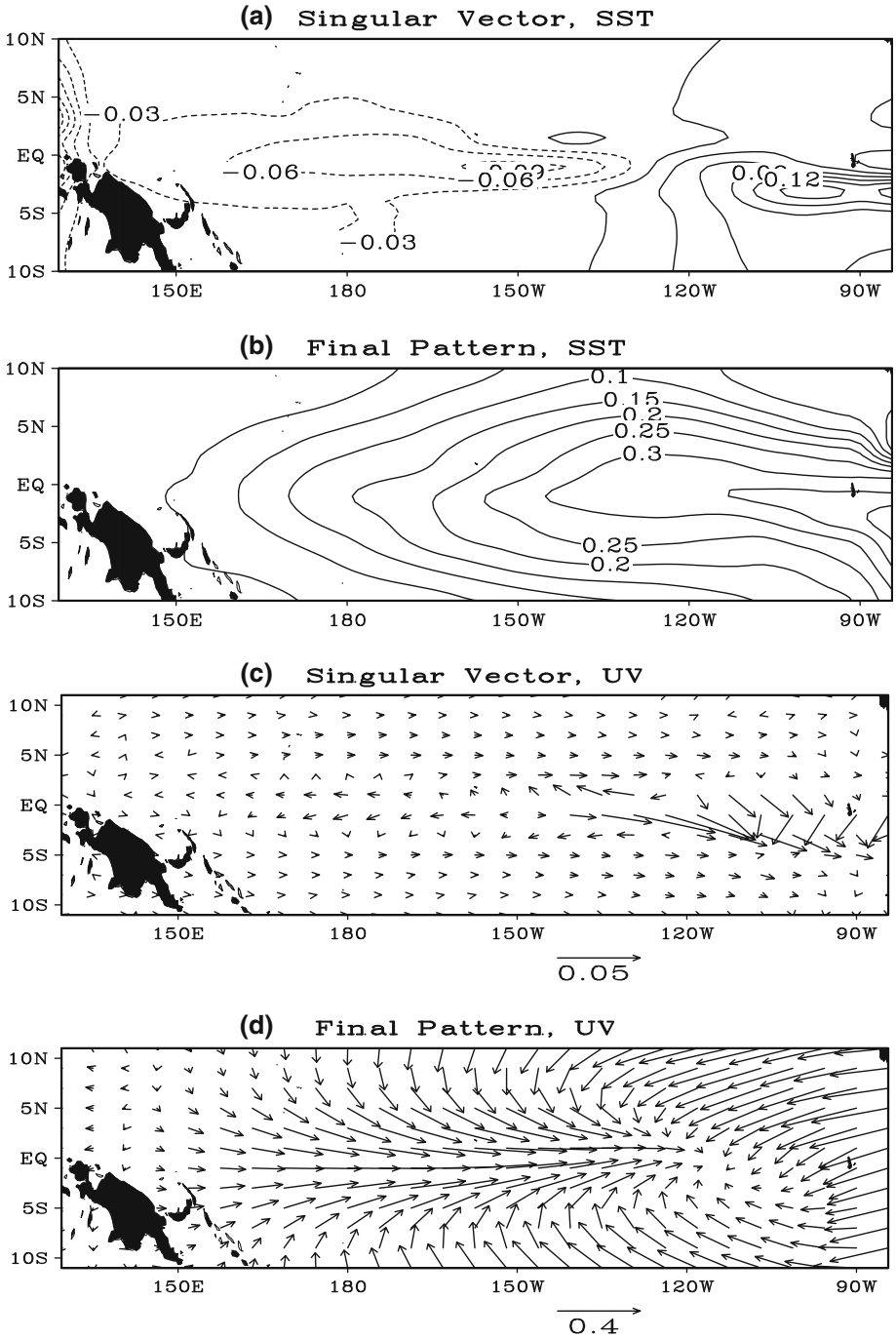

Fig. 2 Same as Fig. 1 but perturbing both SSTA (°C) and wind field (m/s). **a** The first singular vector of SSTA. **b** The first final pattern of SSTA. **c** The first singular vector of the wind field. **d** The first final pattern of the wind field

meridional wind V). The initial perturbation of winds is 0.05 m/s in Fig. 2c. The results show that the spatial distributions of the new SV1 (Fig. 2a) and the final pattern of SSTA (Fig. 2b) are similar to those shown in Fig. 1(a, b), indicating the SV1 and the final pattern of SSTA are mainly determined by the uncertainty in SST itself. This similarity is because the stochastic atmospheric noise is not included in the ZC model and uncertainties in winds are highly related to those in SST, thereby, they can be well represented by SST uncertainties. The adjustment of the atmosphere to ocean variables such as SST and upper ocean heat content is fast, making the atmosphere a "slave" to the ocean at monthly or longer time scales. Warm SST causes atmospheric convection, resulting in a convergence of mass in the atmosphere on both sides of the equator as shown in Fig. 2c, the SV1 of winds. Correspondingly, the final pattern of winds shows a strong association with El Niño. For example, large westerly wind anomalies prevail over the central equatorial Pacific. The close relationship between SST and the surface wind stress

over the tropical Pacific has been documented in many studies. The tropical atmosphere responds to large-scale SST anomalies in a coherent and reproducible way; the tropical flow patterns, especially over the open ocean, are so strongly determined by the underlying SST that they show little sensitivity to changes in the initial conditions of the atmosphere (e.g., Stern and Miyakoda 1995; Shukla 1998). Vialard et al. (2005) performed a series of ensemble forecasts by the European Centre for Medium-Range Weather Forecasts (ECMWF) seasonal forecasting system using wind, SST perturbation and random perturbation to the atmosphere during the forecast, individually and collectively. Their results suggested that the uncertainties in SST determine the spread of ensemble forecasts during the first 2 months of the forecast, while perturbations of the wind stress or atmospheric internal variability alone underestimate the perturbation growth during the early months of the forecast. Therefore these results suggest that ENSO predictability depends more on initial conditions in SST than in atmospheric winds. However, the air–sea coupled components are much deterministic than the uncoupled atmospheric noise, thus, to a certain extent, uncertainties are supposed to be originated from such noise. Because the atmospheric noise component is not fully considered in the ZC model, it leaves room to improve the ENSO predictability by including stochastic atmospheric noise. A more useful forecast strategy might be to perform ensemble predictions and evaluate the uncertainties of the forecast system and ENSO predictability using probabilistic methods (Chen and Cane 2008). And the SV method is one of the widely used ensemble construction methods to generate the probabilistic weather forecasts.

It has been found in previous work that the SV1 is not sensitive to initial conditions in many models (i.e., Chen et al. 1997; Xue et al. 1997a). It is of interest to further explore the sensitivity of SV1 to initial conditions using a long-term analysis. To do this, we calculated spatial correlations between the 148-year averaged SV1 and each individual SV1, which measures the similarity among individual SV1s. The result is shown in Fig. 3. For most cases (over 80%), the spatial correlation coefficients are over 0.80, with an overall average of 0.85 for all initial conditions (148 × 12 months). Even though the majorities (80%) of SV1s are similar, it is interesting to know the differences of initial patterns for those (20%) SV outliers from majority SVs. Composite maps of SV1 are made for those 80% and 20% cases, as shown in Fig. 4(a, b), respectively. As can be seen in Fig. 4, the difference between the two SV1 patterns is small, only manifested in the equatorial western Pacific. The strong spatial similarity in Fig. 3 and small difference in Fig. 4 indicate that SV1 is

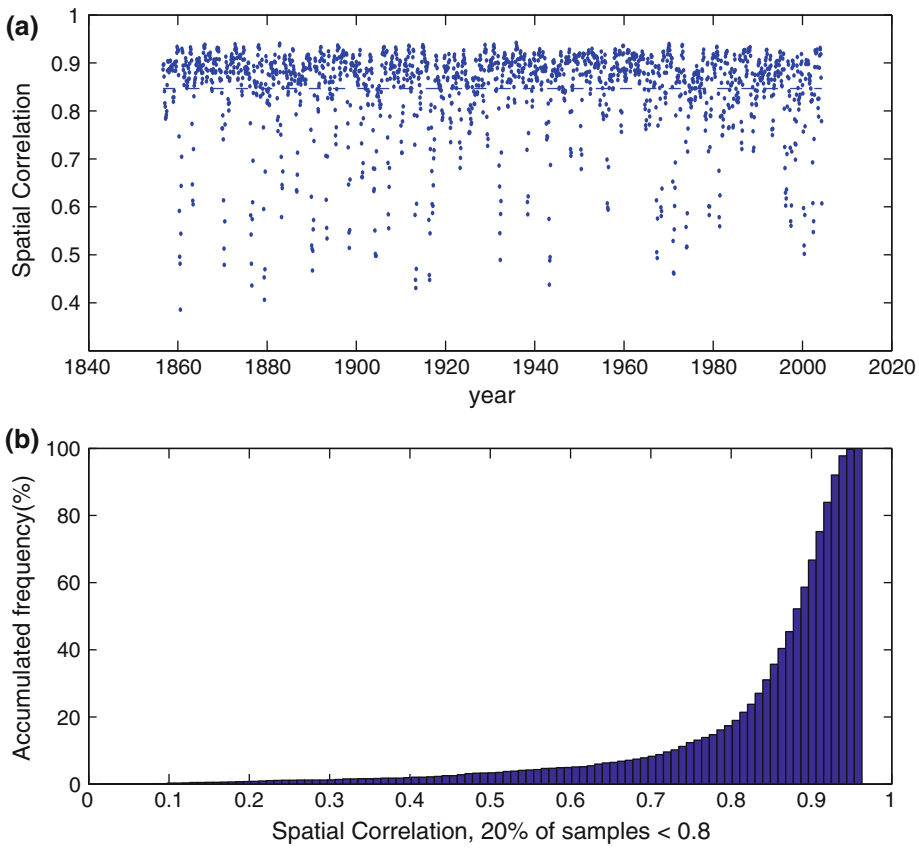

Fig. 3 **a** Spatial correlation coefficients between each first SV over 148-year and the averaged SV-1, the mean correlation coefficient is 0.85 (*dash line*). **b** Accumulated frequency against the spatial correlation coefficient. It indicates the fraction of SVs that is smaller than the spatial correlation coefficient. For example, 20% of SV samples have the spatial correlation less than the spatial correlation of 0.8

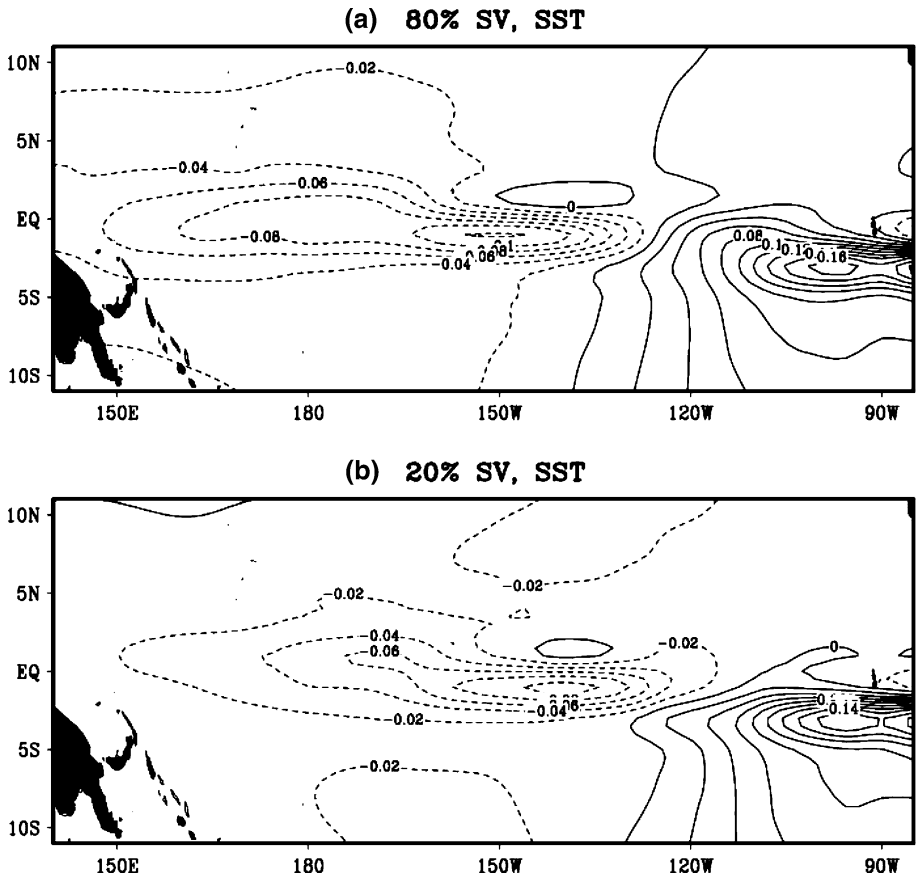

Fig. 4 Composite SV1 of SSTA (°C) for **a** high spatial similarity cases (80% of total SV1) and **b** low spatial similarity (20% of total SV1)

indeed insensitive to initial conditions in the ZC model. A stable SV1 pattern will be useful in ensemble construction to improve the resolution of ensemble-based probabilistic forecasts.

SV1 is also insensitive to the background SST of the ENSO phase. Based on a threshold of ±0.5°C of NINO3.4 SSTA (SSTA over the region 5°S–5°N, 120°W–170°W), El Niño and La Niña events are defined when the threshold is met for a minimum of five consecutive months. The peak phase and the onset phase of La Niña are further defined by NINO3.4 SSTA <-1.2°C and -0.5°C $<$ NINO3.4 SSTA -1.0°C, respectively. The neutral ENSO state, onset of El Niño, and the peak El Niño phase are defined by |NINO3.4 SSTA| <0.5°C, 0.5°C < NINO3.4 SSTA <1.0°C, and NINO3.4 SSTA >1.5°C, respectively. For each stage, a composite SV1 and a corresponding final pattern over 148 years are presented in Fig. 5. All SV1s in different ENSO stages have a similar west–east dipole pattern in the equatorial Pacific and with very similar amplitude. The spatial coverage of final patterns, however, slightly varies with ENSO phases. As seen in Fig. 5(b2–d2), at the onset and neutral ENSO stages, final patterns span over almost all the equatorial Pacific; whereas at peak ENSO stages final patterns shrink and are confined to the east side of the dateline. Figure 6 shows the SV1 of thermocline depth anomaly (H) and their final patterns for different ENSO phases. Similar to SSTA, the leading SV mode of thermocline is not sensitive to ENSO background, as expected. After 6 months, the final patterns show some differences among ENSO phases, although the major features remain consistence, i.e., thermocline deepening in the east and shoaling in the west.

It is of interest to explore the variability of SV1 and final pattern at interdecadal time scales. Based on the prediction skill presented in Chen et al. (2004) and Tang et al. (2008), we selected two 40-year SV1s and final patterns from the 148-year SV1 results. The model forecast correlation skill in the 40-year period of 1876–1895 and 1976–1995 was high; and another 40-year period is 1916–1955, with a low correlation skill. It was found that the composite SV1 and final pattern in two high prediction skill periods are very similar to each other with the averages shown in Fig. 7(a, c). As expected, the SV1 of 1916–1955 shown in Fig. 7b is also very similar to Fig. 7a due to the fact that SV1 is not sensitive to initial conditions. In contrast to this time invariant feature of SV1, final pattern changes significantly between high and low prediction skill periods. As seen in Fig. 7, the final pattern has a weaker perturbation growth amplitude and a smaller spatial coverage in the high correlation skill period; final pattern in the low correlation

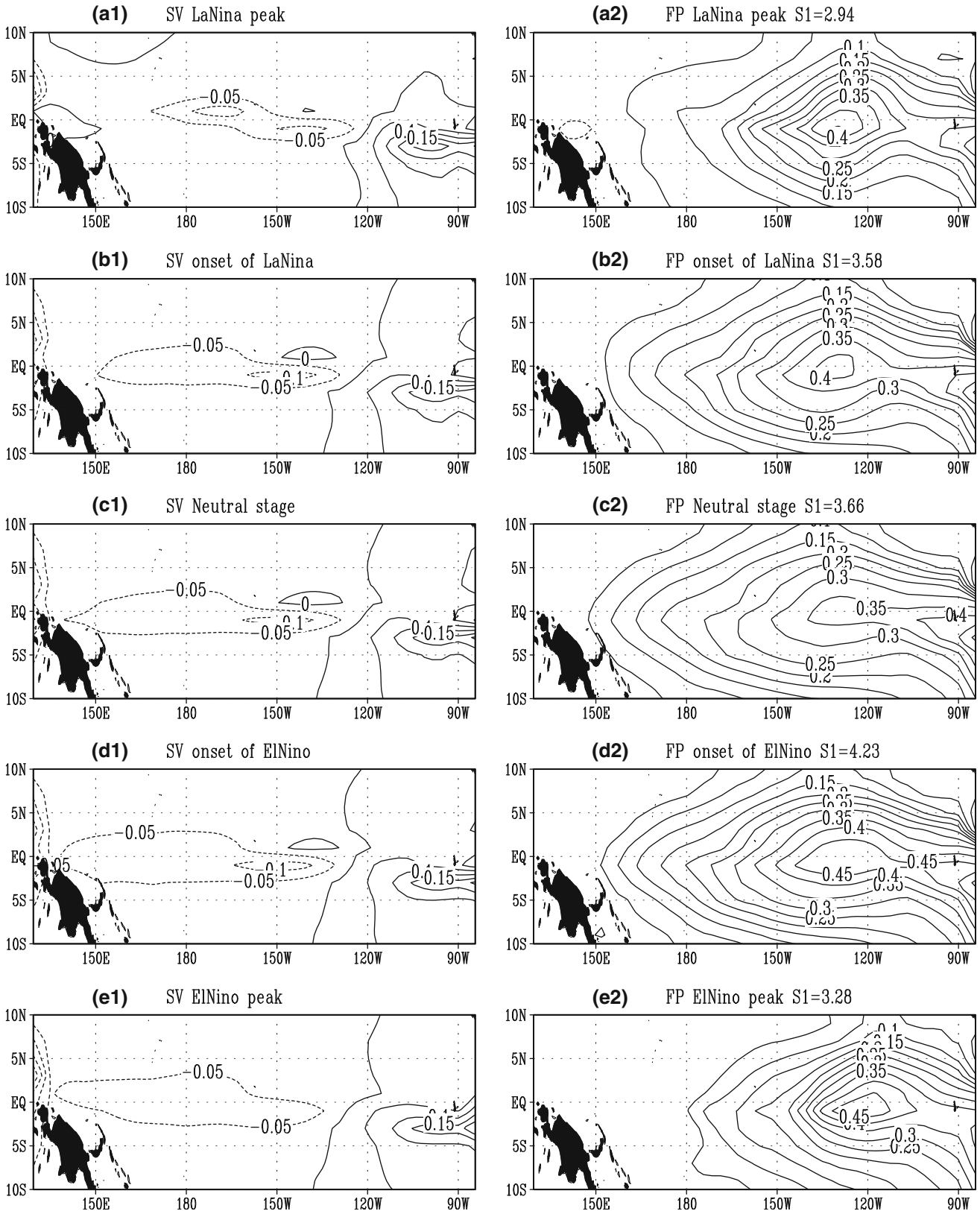

Fig. 5 The first SV of SSTA (°C) starting from the phase of **a1** peak La Niña; **b1** onset of La Niña; **c1** Neutral; **d1** onset of El Niño; **e1** Peak El Niño. The corresponding final pattern after 6 months is shown in the *right panel* **a2**–**e2**. The averaged perturbation growth rate S1 of each stage is marked in the title captions

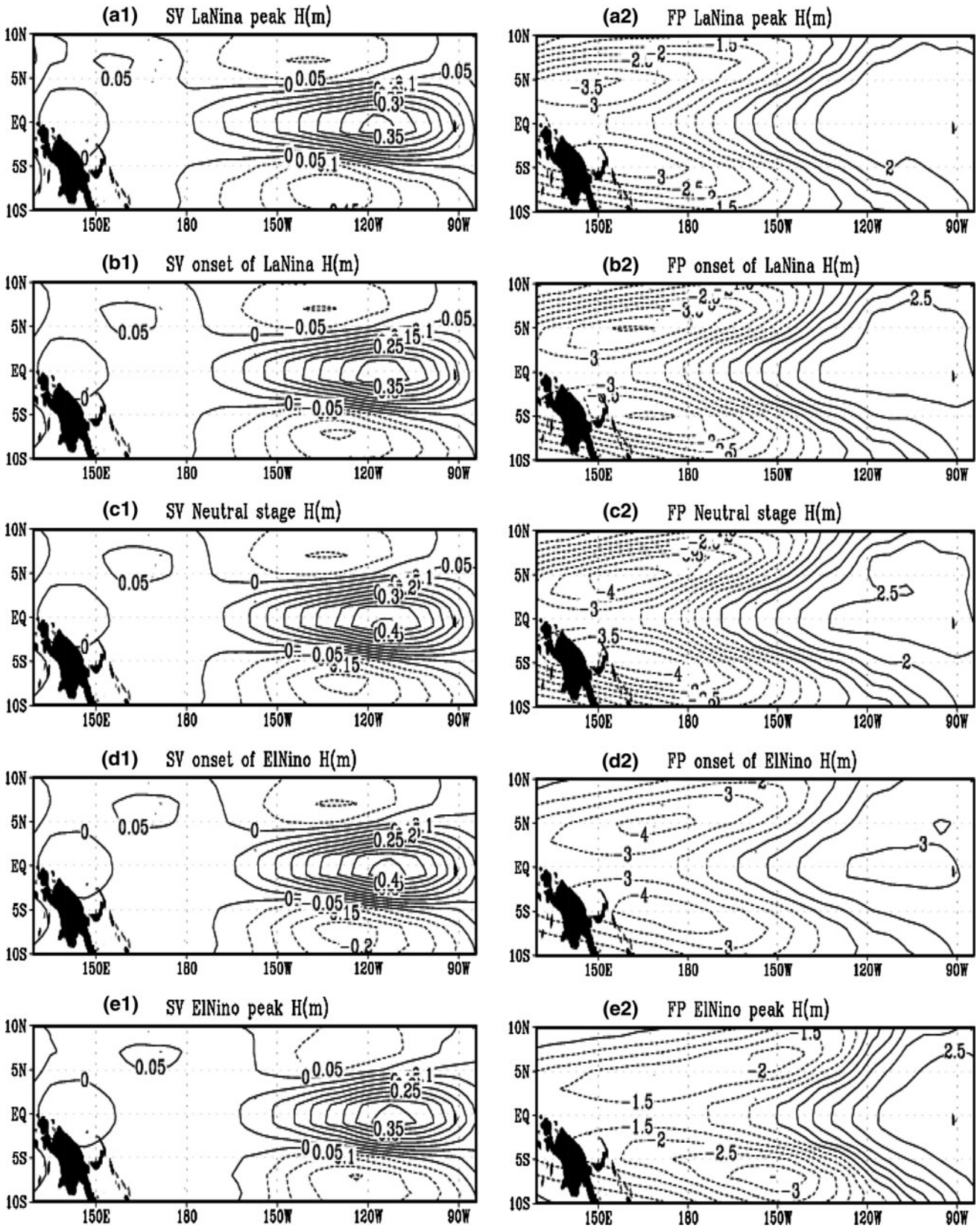

Fig. 6 Same as Fig. 5 but for thermocline depth anomaly (H) (unit: m)

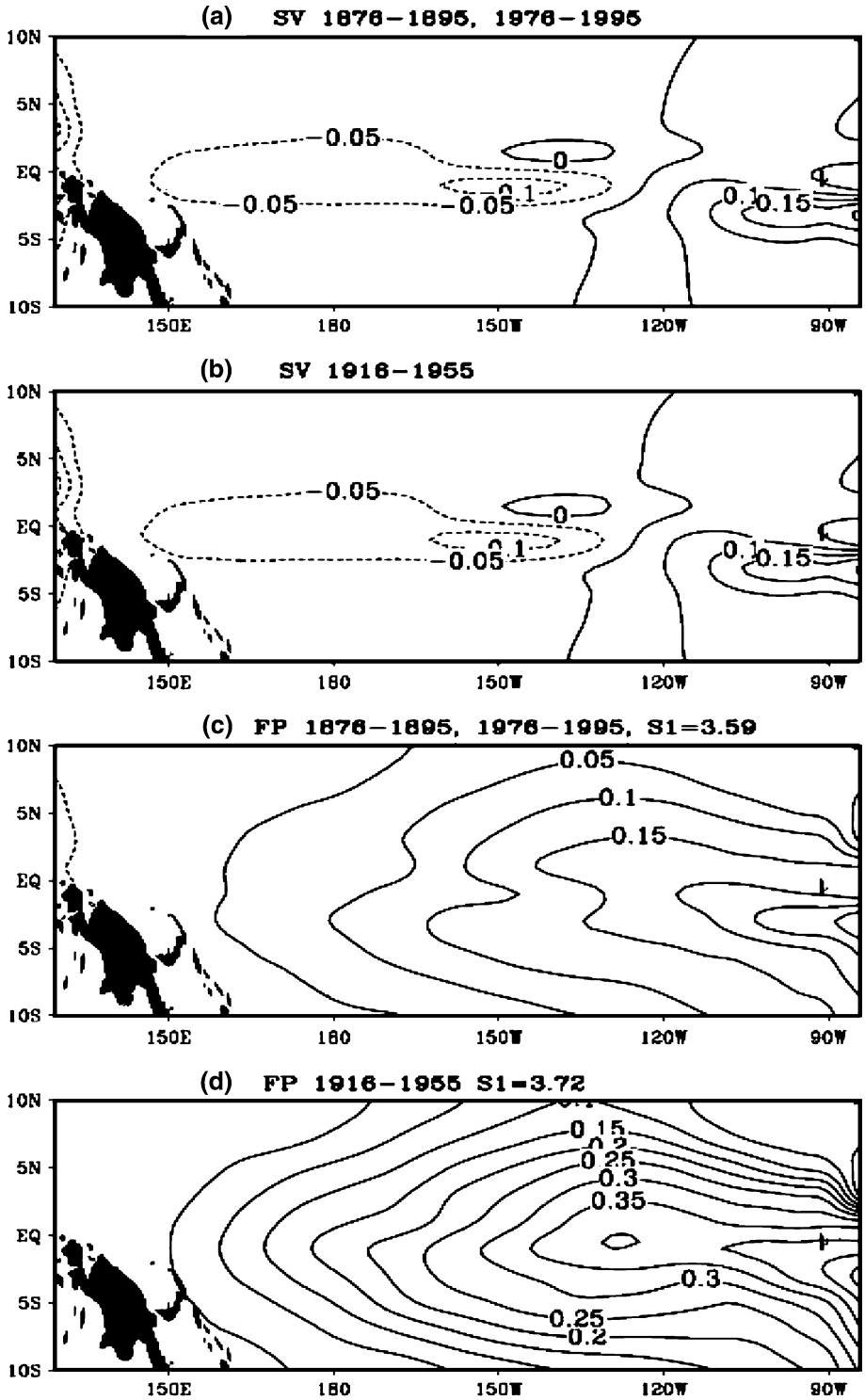

Fig. 7 **a** The SV and **b** the final pattern (FP) averaged in the higher skill period (1876–1895 and 1976–1995) and **c** SV and **d** the final pattern in the lower skill period (1916–1955)

skill period is more than twice as large as the final pattern in the high skill period. Therefore, there is an inverse relationship between the prediction skill of the model and the amplitude of final pattern on the interdecadal time scale.

3.2 Variations of the singular value

The first singular value (S1) represents the fastest perturbation growth rate. Shown in Fig. 8 are the 148-year averaged S1s over all initial conditions for different

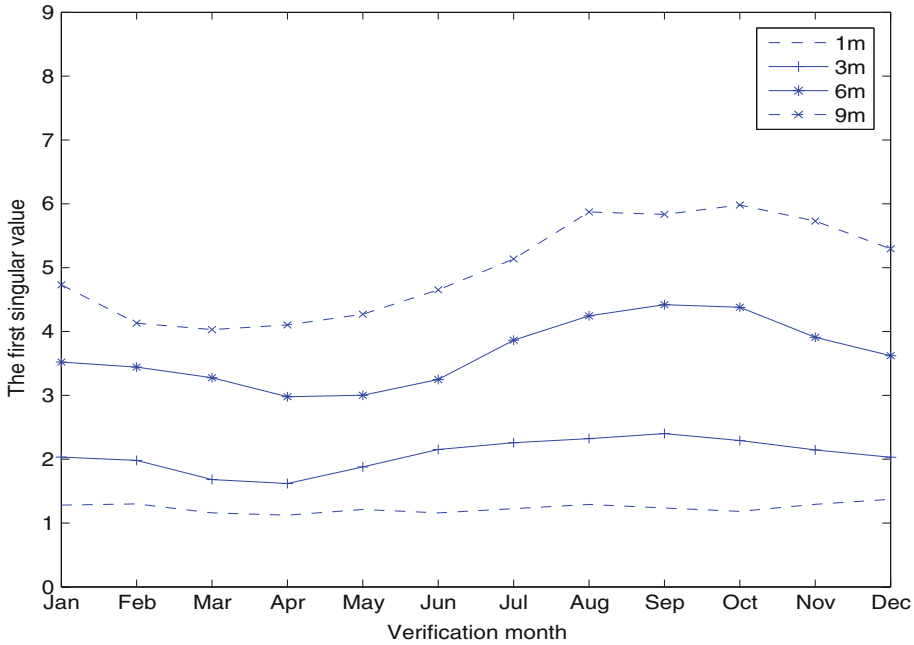

Fig. 8 Seasonal variations of the first singular values S1 against the prediction target time at different lead time, 1, 3, 6 and 9 months (from *bottom* to *top* respectively) averaged over 148 years

calendar months and lead times (1, 3, 6 and 9 months). Note that in Fig. 8, S1s are from the SV analysis with perturbation of only SSTA. The amplitude of S1s with perturbations of both the SSTA and anomalous winds is almost the same as that of Fig. 8, therefore, not shown here. As can be seen in Fig. 8, large S1s often occur at their verification time (the end of the forecast) from August to October in corresponding predictions starting in the boreal spring or summer. For example, the maximum S1 occurs in September or October for 3, 6, and 9-month leads, corresponding to the starting month of June, March and February, respectively. This seasonal dependence in perturbation growth might explain why ENSO prediction skill often drops remarkably when prediction periods start from the boreal spring and pass through the boreal spring and summer, i.e., the 'Spring Barrier'. Jin et al. (2008) recently performed 22-year retrospective ENSO predictions using 10 different coupled GCMs. Their results show that the skill of forecasts that start in February or May drops faster than that of forecasts that start in August or November because predictions starting from February or May contain more events in the decaying phase of ENSO. Based on dynamics, the "Spring Barrier" is probably due to the fact that the Intertropical Convergence Zone (ITCZ) is closest to the equator during the spring, sustaining the unstable condition, whereas the ocean–atmosphere interaction is strong during the summer due to the relatively large vertical temperature gradient and ocean upwelling (e.g., Xue et al. 1997a). In addition, Fig. 8 shows that the magnitude of S1 increases with the lead time as expected.

It is interesting to explore whether S1 shows interannual or even longer time scale variability given the existence of decadal/interdecadal variations of ENSO prediction skill (e.g., Kirtman and Schopf 1998; Tang et al. 2008; Chen et al. 2004). A low-pass filter (2-year) based on the Fourier transform (FFT) has been applied to the S1 of 6-month leads and the NINO3.4 SSTA index to address interannual and longer signals. The two filtered time series are shown in Fig. 9(a, b). As can be seen, they have both visible interannual and longer time scale variability. The interannual and decadal/interdecadal variability of S1 and the NINO3.4 SSTA index can be further verified by the wavelet analysis shown in Fig. 9(c, d). The local significant period varies between 2 and 20 years during the whole period from 1856 to 2003, including the ENSO interannual time scales (2–8 year) and the decadal/interdecadal modulation of ENSO. On the interannual time scale, the significant time period of S1 tends to shift from a longer time scale to a shorter time scale. For example, the significant time period shifted from 8-year to 3-year between 1870 and 1900; this phenomenon reoccurred between 1900 and 1960. When comparing Fig. 9c with the wavelet power spectrum of the NINO3.4 index in Fig. 9d, similar shifting characteristics are found indicating that the changes in the significant periods of the perturbation growth rate was associated with changes in the ENSO signal (spectrum power of NINO3.4) on the interannual time scale. It also indicates that ENSO tended to happen more frequently in recent decades and has a higher frequency of error occurrence. However, on the decadal/interdecadal time scales, Fig. 9(c, d) show that the power spectrums of S1 and NINO3.4 were not consistent in most of the time period except during the time period of 1900–1920 and around 1980. ENSO decadal/interdecadal signals were relatively

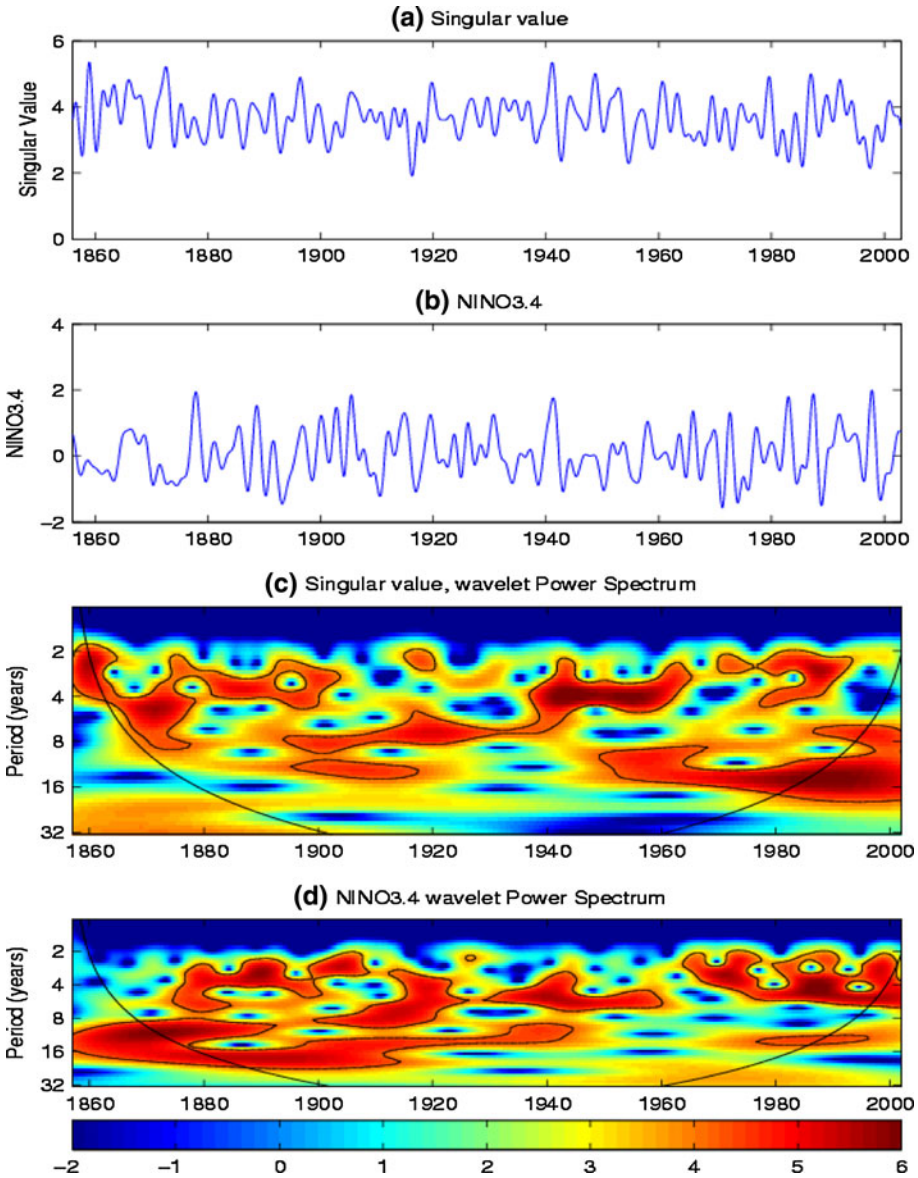

Fig. 9 Time series of the low-pass filtered (>24 months) **a** the first singular value (S1) and **b** the NINO3.4 index used for the wavelet analysis. Wavelet power spectrum of **c** S1 and **d** NINO3.4 using the Morlet wavelet. The thick contour encloses regions of greater than 95% confidence, using a red-noise background spectrum. The *solid smooth curves* in the left and right corners indicate the edge effects become important

weak between 1945 and 1975 while the spectrum power of the perturbation growth was significantly stronger over this period.

To examine relationships between NINO3.4 SSTA index and the S1, in particular their local relative phases, in time frequency space, the cross-wavelet analysis method (Grinsted et al. 2004) is applied for Nini3.4 SSTA and S1. The temporal variation of cross wavelet power spectrum is shown in Fig. 10, where the relative phase relationship is shown as arrows, with in-phase pointing right, anti-phase pointing left, and NINO3.4 SSTA index leading S1 by 90° pointing straight down. As can be seen, both the phase synchrony and phase asynchrony between the two series can be observed at different time scales from decades to decades. For example, in-phase relationships are visible at the interannual time scales from 1880–1920 and 1940–1950 whereas the anti-phase relationships occurred at decadal/interdecadal time scales from 1900–1940 and 1960–1980. The anti-phase feature at decadal/interdecadal scales is in agreement with the ENSO predictability study in Tang et al. (2008) using multiple models, where they found that at decadal/interdecadal scales, strong ENSO events were related to small perturbation growth rates and vice versa. In addition, at interannual time sales, the significant periods seem gradually shifted to shorter scales from 1880 to 2000, which is probably due to the enhancement of ENSO variability in amplitude and frequency with time during the past 100 years. We will further discuss the relationships between ENSO signals and perturbation growth rate in part II of this work.

Many recent 20–30 years interval SV analyses concluded that: (i) a small perturbation growth rate often

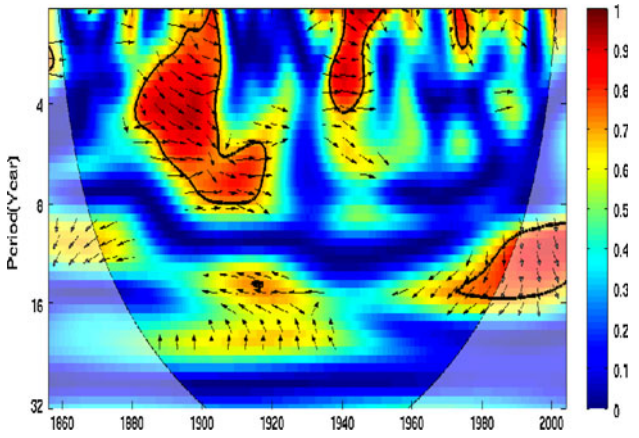

Fig. 10 The cross-wavelet analysis for NINO3.4 SSTA index and the singular value S1. The thick contour encloses regions of greater than 95% confidence, using a red-noise background spectrum. The relative phase relationship is shown as *arrows*, with in-phase pointing *right*, anti-phase pointing *left*, and NINO3.4 SSTA index leading S1 by 90° pointing *straight down*

occurs during an ENSO peak phase; and (ii) the larger perturbation growth rate shows in the neutral and onset/breakdown stages of ENSO (Chen et al. 1997; Xue et al. 1997a; Tang et al. 2006; Zhou et al. 2007). Cai et al. (2003) obtained similar results when they analyzed the perturbation growth rate of the ZC model using a very long period breeding vector analysis. For comparison, we examined the above features of perturbation growth rate and ENSO phase over 148 years, resulting in a similar plot to Fig. 5 in Cai et al. (2003), as shown in Fig. 11. The ENSO events are binned into 18 categories between −2°C and 2.5°C with a 0.5°C interval based on the NINO3.4 SSTA index or NINO3 SSTA index (5°S–5°N, 90°W–150°W). The mean S1 of each category is shown as a function of the ENSO phase and the SSTA tendency. As shown in Fig. 11a, where 18 bars represent the 18 categories from the left to right. Bins 1–9 have positive tendencies of SSTA and bins 10–18 have negative tendencies. In addition, bins 1–3 and 16–18 are at cold ENSO phase, bins 4–5 and 14–15 are at neutral phase, and bins 6–13 are at warm phase. The small perturbation growth rate occurs at the peak ENSO stage (peak El Niño and La Niña, bins 8–10 and 1, 18, respectively). While the large perturbation growth occurs prior to the decay phase of El Nino (bins 11–13) and during the transition period from a cold to a warm state (bins 3–5). These results are generally consistent with former SV studies (e.g., Chen et al. 1997; Xue et al. 1997a) and breeding vector results (e.g., Cai et al. 2003; Tang and Deng 2009) and further confirm the sensitivity of perturbation growth on ENSO phase. In the next section, we will identify and investigate the possible physical processes controlling the perturbation (error) growth in the ZC model.

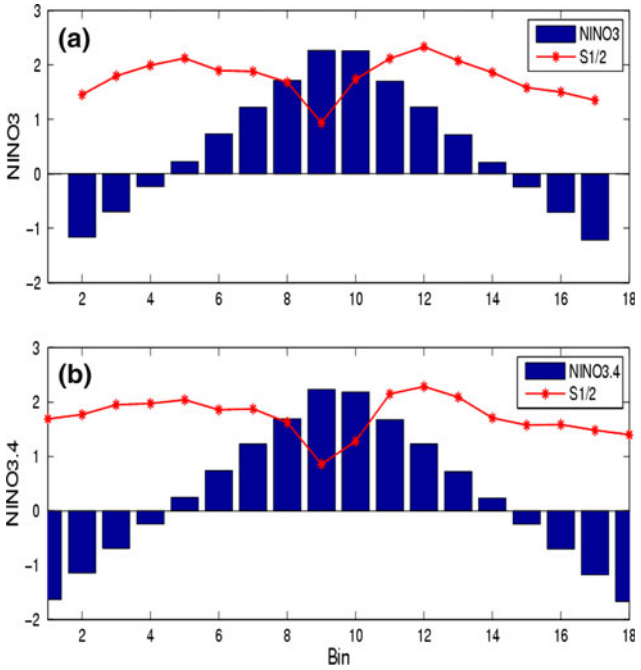

Fig. 11 Mean S1 (in *solid star curve*) as a function of the background ENSO phase. **a** The *bar curve* is the NINO3.4 index of the composite background ENSO cycle (S1 is divided by 2); **b** same as **a** but using NINO3 index

4 Physical processes of perturbation growth in the ZC model

The evolutions of the model initial perturbations and ENSO signals are simultaneously controlled by internal dynamical and thermodynamical processes of the model such as the horizontal advection and vertical mixing. To explore underlying physical processes of the model perturbation growth, we decomposed the model SSTA variations into linear terms and nonlinear terms following the definition of An and Jin (2004), and performed several sensitivity experiments of SV analysis to investigate the contribution of individual term to the original total perturbation growth.

The governing equation of SSTA in the ZC model can be written as below

$$\frac{\partial T'}{\partial t} = -\overrightarrow{\overline{U}} \cdot \nabla T' - U' \cdot \nabla(\overline{T} + T') - [M(\overline{W} + W') - M(\overline{W})]\frac{\partial \overline{T}}{\partial Z} - M(\overline{W} + W')\frac{\partial T'}{\partial Z} - \alpha T' \quad (9)$$

where $T'(\overline{T})$, $U'(\overline{U})$, and $W'(\overline{W})$ are anomalies (mean) of SST, surface layer currents, and vertical velocity, respectively, and α is a thermal damping coefficient. The first two terms on the right hand side of (9) are the horizontal advection terms. The third and fourth terms represent the effects of anomalous upwelling in the presence of the mean vertical temperature gradient $\frac{\partial \overline{T}}{\partial z}$, and the total upwelling in the presence of the anomalous vertical temperature

gradient $\frac{\partial T'}{\partial z}$, respectively. The final term is a linear damping term, which can be interpreted as the change of SSTA due to the heat exchange between ocean and atmosphere. $M(x)$ is a step function: $M(x) = x$ if $x \geq 0$; $M(x) = 0$ if $x < 0$ which brings a cooling effect when there is upwelling and no effect otherwise since downward motion causes no change in SSTA.

If we consider the linear and nonlinear heating effects of horizontal advection and vertical advection (upwelling or downwelling), Eq. 9 can be expressed as:

$$\begin{aligned}\frac{\partial T'}{\partial t} = &-\overline{u}\cdot T'_x - u'\overline{T}_x - \underline{u'T'_x} - \overline{v}T'_y - v'\overline{T_y} - v'T'_y \\ &-M(\overline{w})T'_z - \underline{\{M(\overline{w}+w') - M(\overline{w})\}\overline{T_z}} \\ &-\underline{\{M(\overline{w}+w') - M(\overline{w})\}}T_z{}' - \alpha T'\end{aligned} \tag{10}$$

where T, u, v, and w are SST, zonal, meridional, and vertical current velocities, respectively. The overbar and prime denote the climatological mean and anomaly, respectively. The underlined terms are nonlinear heating (NH) and the remaining terms are linear heating (LH), following the definition of An and Jin (2004). The linear and nonlinear heating terms can further be subdivided into the horizontal linear (HL), the horizontal nonlinear (HN), the vertical linear (WL), and the vertical nonlinear (WN), respectively. The linear dumping term is considered in the horizontal linear term (HL).

To identify the contribution of each individual heating term to the original perturbation growth, we performed SV analysis for each linear and nonlinear term over 148 years respectively. Note that the nonlinear heating terms have been linearized in the TLM, the nonlinear perturbation/perturbation growth mentioned hereafter are actually the linearized nonlinear perturbation contributions. The SV analysis of each term is similar to the original analysis described in Sect. 2.2 except that the perturbation growth of SST (i.e., X_f in Eq. 7) was replaced by the perturbation growth of an individual heating term obtained from the TLM. This is confirmed by the results obtained using tangent linear model (7), where the original SV1 is used as initial condition X_i for integration of TLM. It was found that SV1s of these heating terms are similar to the original SV1 as shown in Fig. 1a. This is because the solution of maximizing total perturbation growth rate A in (4) is equivalent to the solution of maximizing growth rate of each individual term. The final patterns of these terms are subject to their physical processes, representing the perturbation contribution from each heating term. The final pattern of each term from SV analysis is actually equivalent to the response of corresponding term (X_f) to the original SV1 (X_i) by (7). The 148-year averaged final patterns for the linear and nonlinear terms are given in the left and the right panel of Fig. 12, respectively. The final pattern of the total horizontal linear heating (Fig. 12e) is very similar to the original final pattern in Fig. 1b. There are two positive perturbation growth regions in the tropical equatorial Pacific, located in the central Pacific Ocean and the eastern Pacific, respectively. The former center in the central Pacific near 150°W, where the strong atmosphere–ocean interactions and large instability conditions often occur, is formed as a result of the horizontal linear perturbation growth (see Fig. 12a). The perturbation growth in the eastern Pacific is clearly related to the vertical linear term (Fig. 12c), indicating that the optimal growth in the eastern Pacific Ocean is mainly due to the vertical linear upwelling/downwelling term. This vertical linear optimal growth is probably due to an inaccurate parameterization of the vertical mixing process. The high spatial similarity of the final patterns of the total linear and horizontal linear optimal growth suggests the linear heating perturbation growth dominates the total model perturbation growth. However, if we ignore the perturbation contribution of the nonlinear process, the perturbation growth in the central Pacific would be much stronger than the perturbation growth in the original final pattern. This large perturbation growth in the linear process implies that there must be some offset effects (negative optimal growth) in the total nonlinear heating processes that reduce the large linear perturbation growth. We can see this reduction in the total nonlinear perturbation in Fig. 12f: there is a negative perturbation growth center in the central Pacific near the dateline region where it can partly offset the positive perturbation growth in the total linear perturbation. Therefore, both the linear perturbation growth and nonlinear perturbation growth are important in the central Pacific. The total nonlinear error can be further decomposed by the horizontal nonlinear term and the vertical nonlinear term shown in Fig. 12(b, d). There is a large negative perturbation growth region in the central Pacific in the horizontal nonlinear term, which is similar to the total nonlinear perturbation growth pattern shown in Fig. 12f; meanwhile, a relatively weak positive perturbation growth is shown in the vertical nonlinear term in the central Pacific (Fig. 12d). Therefore, the total nonlinear negative error is mainly the result of the horizontal nonlinear term. Comparing Fig. 12e with f shows the perturbation growth contribution of the total linear heating is 3–4 times larger than the contribution of the nonlinear heating (note that the perturbation growth rates were included in FPs). Therefore, total model errors are mainly caused by the linear advection heating process, but the linear process can be partially offset by the nonlinear process which has a negative error contribution, especially in the central Pacific.

To compare the error contributions of individual linear/nonlinear heating terms, the seasonal variations of these perturbation growth rates are given as a function of the forecast verification time (Fig. 13). As expected, the

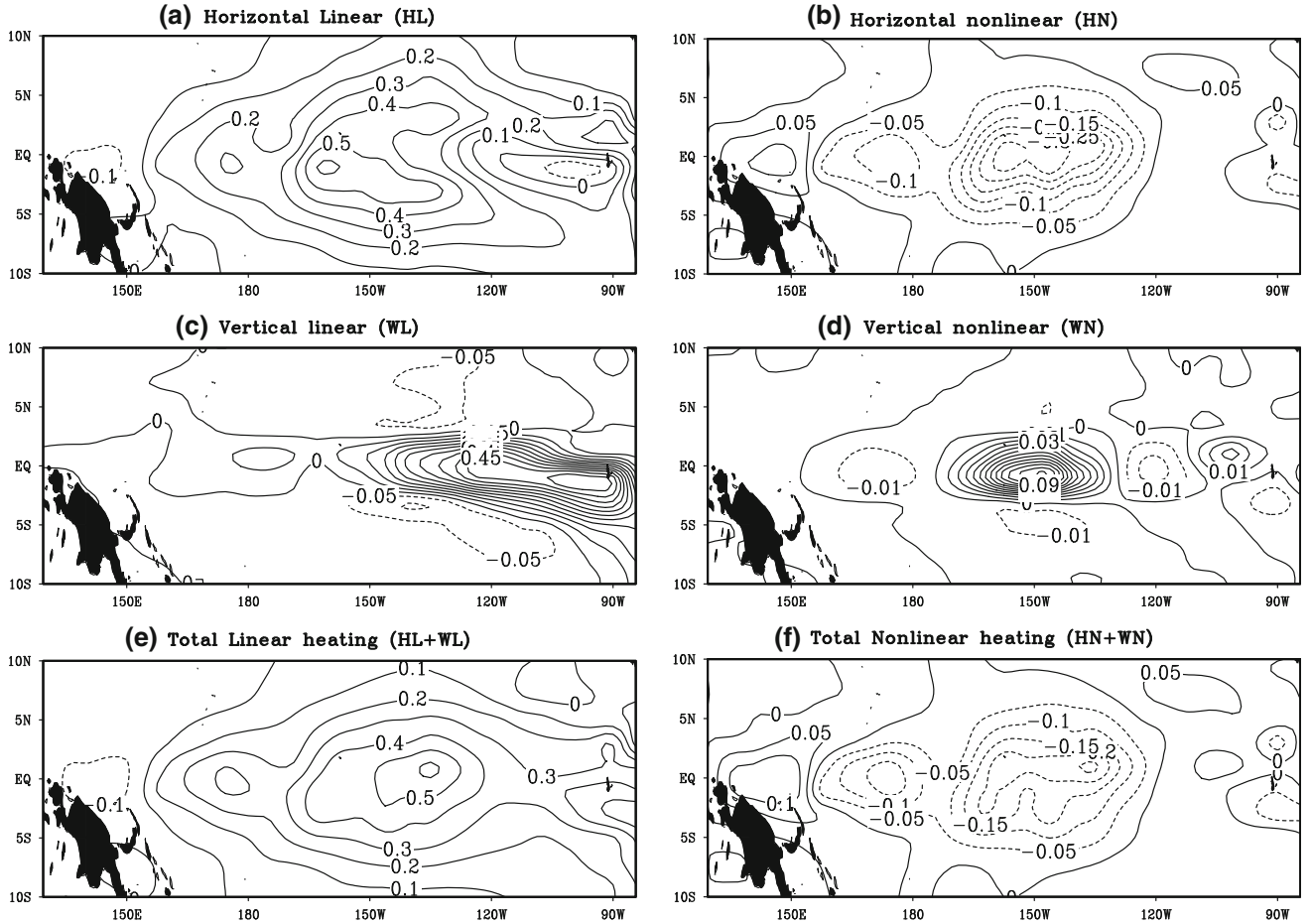

Fig. 12 Final patterns for linear and nonlinear heating terms averaged in 148 years. **a** The final pattern of horizontal linear heating (HL). **b** The final pattern of horizontal nonlinear heating. **c** The final pattern of vertical linear heating (WL). **d** The final pattern of vertical nonlinear heating(WN). **e** The final pattern of total linear heating (HL + WL). **f** The final pattern of total nonlinear heating (HN + WN). (Unit: °C)

horizontal linear heating term (HL) makes the largest contribution to the original growth rate S1, and shows a consistent seasonal variation with original perturbation growth S1. The vertical linear heating (WL) and horizontal nonlinear heating (HN) have comparable error contributions, but they are much smaller than horizontal linear perturbation growth (HL). Comparing the vertical nonlinear perturbation growth (WN) with the other three terms shows that the vertical nonlinear perturbation growth is the smallest contributor with very weak seasonal variations. To visualize the linear and nonlinear error contributions more clearly, seasonal variations of the perturbation growth rates are given in Fig. 13b. The perturbation growth of the total linear term is about twice as large as the total nonlinear perturbation growth, which confirms again that the original total perturbation growth S1 is mainly determined by the linear process, and the nonlinear process contributes to a smaller and negative perturbation growth. An offsetting effect between the linear and nonlinear terms explains why the horizontal perturbation growth rate HL is larger than the original perturbation growth rate S1.

To further understand underlying mechanisms of linear and nonlinear perturbation growth, we performed several EOF analyses for individual linear/nonlinear heating terms to look for dominating physical processes that control the variation of total heating, and investigate the relationship between the perturbation growth rate and the corresponding heating term. These individual heating terms were obtained from the integration of the original model again over the period of 1856–2003. For the total linear heating process, the first EOF mode, accounting for 73.1% of total variance, shows an ENSO-like pattern (Fig. 14c). Comparing this EOF mode of total linear heating with the horizontal linear heating (Fig. 14a) and vertical linear heating (Fig. 14b), reveals that the warming in the equatorial central and eastern Pacific is from the contribution of anomalous horizontal linear heating, and the warming along the coastal zone is mainly due to vertical linear

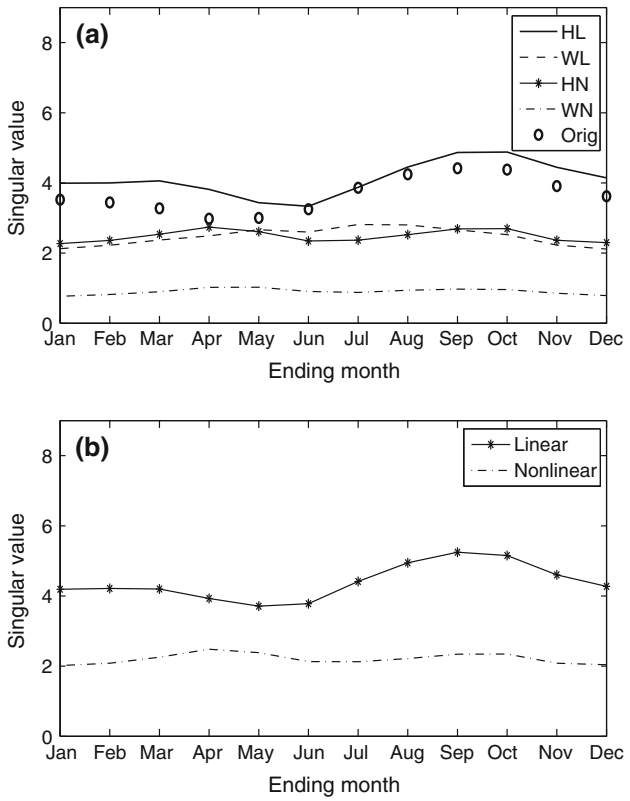

Fig. 13 The seasonal variation of singular values for linear and nonlinear heating terms **a** horizontal linear heating (HL, *solid line*), vertical linear heating (WL, *dash line*), horizontal nonlinear heating (HN, *solid star line*), and vertical nonlinear heating (WN, *dash dot line*). The original singular values (*open circles*); **b** singular values for the linear heating (*solid star line*), nonlinear heating (*dash dot line*)

heating. From the corresponding principal components (PCs) shown in Fig. 14(d–f), linear heating is more likely to cause warming as indicated by dominant positive values in the PCs. Fig. 15(a–c) are the first EOF modes of the horizontal, vertical, and total nonlinear heating terms respectively. Their corresponding PCs are given in Fig. 15(d–f). EOF analyses show a cooling and warming pattern for horizontal and vertical nonlinear terms in Fig. 15(a, b), respectively. Considering that all PCs are positive and that the horizontal nonlinear PC has a larger amplitude than the vertical nonlinear term, the total nonlinear heating NH can be explained by the horizontal cooling effect as shown in Fig. 15c. Xue et al. (1997a) obtained similar results from an older version of the ZC model with a shorter time period, and concluded that the horizontal nonlinear advection is mostly a cooling effect and the vertical advection is mostly a warming effect, namely that, the vertical nonlinear advection always strengthens warm SST anomalies but diminishes cold SST anomalies in the eastern Pacific.

These nonlinear vertical warming and horizontal cooling effects can be further explained mathematically by Eq. 10 together with the final patterns of SSTA and the wind field in Fig. 2. For example, during an El Niño event, the easterly trade wind is weakened and a westerly current anomaly ($u' > 0$) occurs in the central Pacific. Meanwhile, the horizontal SSTA warming increases from the west to the east showing a positive zonal SSTA gradient ($T'_x > 0$). Thus, the horizontal nonlinear advection $\left(-u'T'_x < 0\right)$ contributes a cooling effect in the central Pacific. This horizontal nonlinear cooling effect in the ZC model is in agreement with An and Jin's report (2004) that during the developing phase of El Niño, both the anomalous zonal temperature gradient and the anomalous zonal current in the surface layer are positive, which leads to a negative nonlinear zonal advection. On the other hand, a weakening of upwelling ($w' < 0$) and a stronger warming at the sea surface than in lower layers ($T'_z > 0$) are found in the ZC model (opposite w' and Tz' in observations in An and Jin (2004)). Therefore, the nonlinear vertical mixing $\left(-w'T'_z > 0\right)$ contributes to a warming effect in the central Pacific, which can partly offset the horizontal nonlinear cooling. For La Niña events, in the central Pacific $u' < 0$, $T'_x < 0$ along with a strengthened upwelling, $w' > 0$, and a cooling sea surface $T'_z < 0$. Therefore, the horizontal nonlinear cooling and vertical nonlinear warming are valid.

However, comparing the horizontal and vertical nonlinear heating terms in the ZC model with that from the observations in An and Jin (2004) shows some physical deficiencies of the ZC model: (i) The model's vertical nonlinear term does not show a great enough warming effect to offset the horizontal nonlinear cooling contribution, therefore, the net nonlinear heating is a cooling effect, whereas, in the observations of An and Jin (2004) the vertical nonlinear warming dominates the net nonlinear heating; (ii) The vertical nonlinear warming in the model is located in the central Pacific, while the warming dominated in the eastern Pacific near the cold tongue region in An and Jin (2004); (iii) Although there is an out-of-phase relationship between the upwelling (w') and the vertical temperature gradient $\left(T'_z = \text{SSTA} - T_{\text{sub}}\right)$ through the ENSO cycle in the model, both signs of the vertical motion and the temperature gradient in the model are opposite to observations. The model has a weakening of upwelling ($w' < 0$) in El Niño events and the subsurface warming is smaller than the surface warming $T'_z > 0$. However, there is a strong warm water upwelling occurring in the eastern Pacific in the observations, especially for those strong El Niño events after 1980. An et al. (2005) compared nonlinear heating terms in 10 coupled models and found only one model gave the correct simulation. Most models did not represent both the location and strength or even the sign of the nonlinear vertical warming. This model bias in the internal model dynamics and physical processes certainly will cause perturbation growth but that is beyond the scope of this paper.

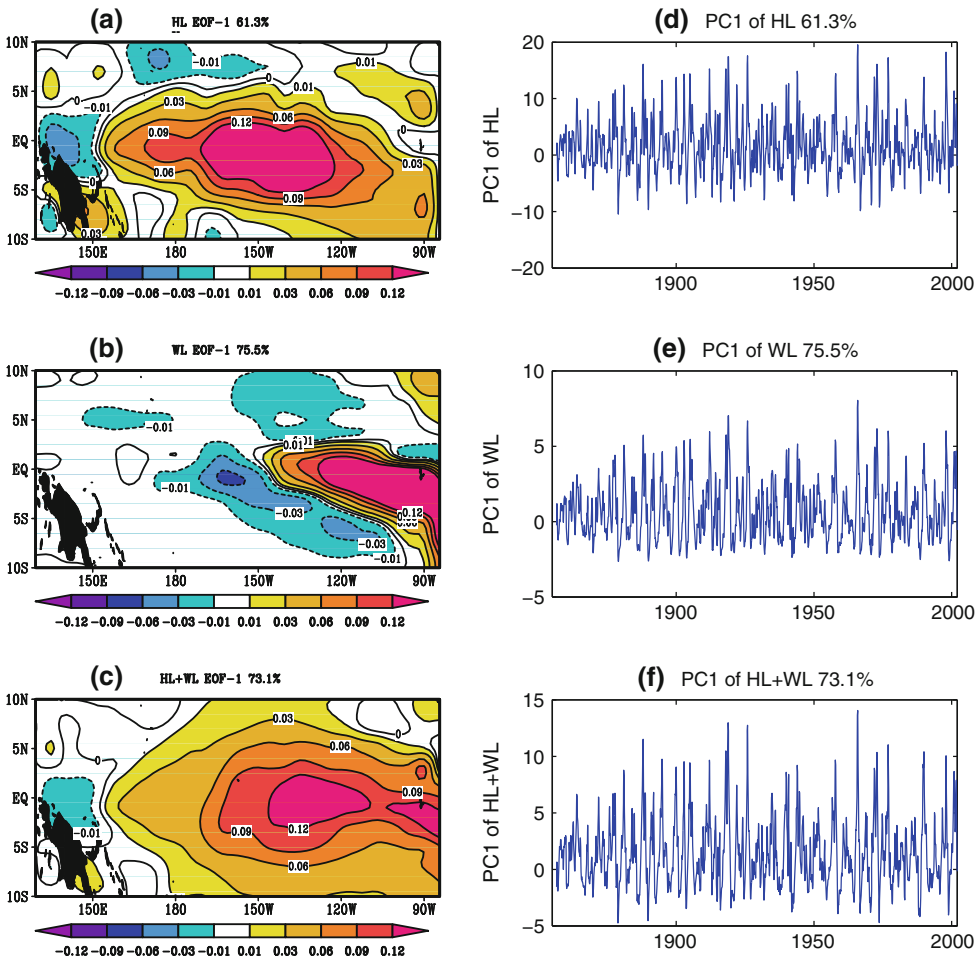

Fig. 14 EOF analyses for linear heating terms in Eq. 10. From *top to bottom*, figures in the *left panel* are the EOF-1 spatial patterns of **a** horizontal linear (HL), **b** vertical linear (WL) and **c** total linear heating (HL + WL). Their corresponding PCs are in the right panel. (Unit: °C/month)

The spatial patterns of linear and nonlinear heating terms revealed by EOF analysis are very similar to their corresponding final patterns of perturbation growth. Furthermore, over 148 years, significant positive correlations have been found between each PC and its corresponding singular value. Strong linear heating is associated with a faster positive perturbation growth while strong nonlinear heating leads to a faster negative perturbation growth. For example, the correlation coefficients between PCs of linear terms HL/WL/total linear and their corresponding singular values are 0.56/0.46/0.44 over 148 years, which are all statistically significant at the 99% confidence level. The correlation coefficients between PCs of nonlinear terms HN/WN/total nonlinear and their singular values are 0.54/0.66/0.46, respectively. Very high spatial similarity and temporal correlations between each perturbation growth rate and the corresponding heating term suggest that the linear perturbation growth (L1) and nonlinear perturbation growth rate (N1) are highly related to the linear/nonlinear physical processes themselves. Comparing Fig. 15 with Fig. 14 reveals that the total linear heating makes a larger contribution to the total heating, leading to the finding that linear processes contribute more to the total perturbation growth than nonlinear processes as found in Fig. 13.

5 Conclusion

It is important to identify a statistically robust SV analysis of ENSO prediction models. The relationship between singular value and ENSO predictability has not been sufficiently addressed in previous studies of ENSO predictability due to a lack of long term retrospective prediction and corresponding SV analysis. In this work, a TLM is constructed for the latest ZC model version LDEO5 to study perturbation growth and ENSO predictability for the past 148 years from 1856 to 2003. It provides a substantial account of the error growth rate and spatial patterns in LDEO5 from seasonal to interdecadal time scales.

From the 148-year singular vector analyses by our new constructed physical-based TLM, the long-term averaged first singular vector SV1 is a west–east dipole spanning the equatorial Pacific with centers located in the east and the central Pacific Ocean. Comparing the SV1 of LDOE5 with

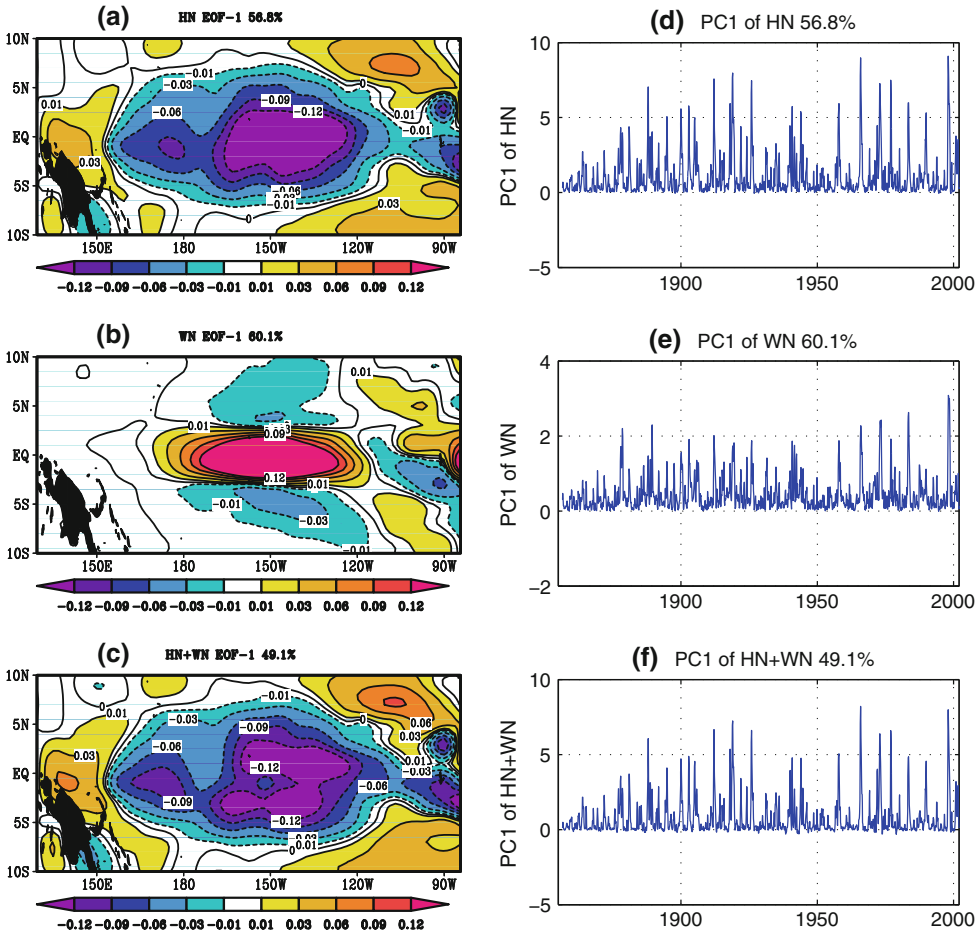

Fig. 15 Same as Fig. 14 but EOF analyses results for nonlinear heating terms. Figures from *top to bottom* are **a** horizontal nonlinear (HN), **b** vertical nonlinear (WN) and **c** total nonlinear heating (HN + WN)

that of the previous SV studies (i.e., Chen et al. 1997; Xue et al. 1997a), we find that the north–south dipole in the older ZC model version in the eastern Pacific is missing, which might be due to improvements in the ZC model (i.e., model dependent). A spatial correlation between the monthly SV1s and the 148-year averaged SV1 agrees with previously published results showing that SV1 is less sensitive to model initial conditions while there is a strong sensitivity of singular values to initial conditions. The faster model perturbation growth during spring/summer is probably caused by the stronger atmosphere–ocean interaction. Besides the seasonal variations, the leading singular value, S1, has significant periods ranging 2–20 years as seen in the wavelet analysis. On the interannual time scales, the significant time scales of S1 and the ENSO signal occasionally shifted from longer periods to shorter periods during the 148 years.

The relative contribution of linear and nonlinear heating to S1 has not so far been addressed well. In this study, we also conducted SV analysis for each individual heating term in the SST governing equation. SV analyses on the individual linear and linearized nonlinear terms reveal that the model optimal perturbation growth is mainly from linear heating terms. The total linear optimal perturbation growth is twice as large as the total nonlinear term. The final optimal perturbation growth pattern of an individual heating term has a similar spatial pattern as the EOF pattern of the heating term. In addition, significant correlations have been found between the perturbation growth rate of each term and corresponding PC-1 of the EOF analysis for the individual heating terms. Therefore, the singular value of each heating term depends significantly on the heating term itself. The perturbation growth in the central equatorial Pacific, where strong atmosphere–ocean interaction occurs, is dominated by a positive perturbation growth from the horizontal linear term. The perturbation growth in the eastern Pacific is dominated by vertical linear mixing, which is probably related to inaccurate parameterization of the mixing process.

A robust and stable optimal error growth pattern, SV1, and the optimal error growth rate, S1, over 148 years will be useful indicators of potential predictability. Further discussion of the relationship between potential predictability that does not use observations, and the model prediction skills indicated by correlation and root mean square error (RMSE) from a comparison

with observations will be presented in Part II of this study. The relationship will offer a practical means of estimating the confidence level of ENSO prediction using the dynamical model. In addition, the SV1s obtained in the present study provide an optimal tool to construct ensemble predictions, i.e., repeating a prediction many times by perturbing the initial conditions of a forecast model with SVs and random noise each time. Through statistical predictability theory and ensemble prediction of the past 148 years, the shape of the forecast probability density function (PDF) that describes the prediction uncertainty can be estimated, and the nature of ENSO predictability explored in part II of this study.

Acknowledgments This work is supported by Canadian Foundation for Climate and Atmospheric Sciences (CFCAS) GR523. Yanjie Cheng is also supported by the Graduate fellowship of NSERC PGS D2-362539-2008. This work benefits from discussions with Dr. Soon-IL An. We also thank Dr. B. P. Kirtman and one anonymous reviewer for their constructive comments.

References

An S, Jin FF (2004) Nonlinearity and asymmetry of ENSO. J Clim 17:2399–2412. doi:10.1175/1520-0442(2004)017<2399:NAAOE>2.0.CO;2

An S, Ham YG, Kug JS, Jin FF, Kang IS (2005) El Niño–La Niña asymmetry in the coupled model intercomparison project simulations. J Clim 18:2617–2627. doi:10.1175/JCLI3433.1

Battisti DS (1988) The dynamics and thermodynamics of a warming event in a coupled tropical atmosphere–ocean model. J Atmos Sci 45(20):2889–2919. doi:10.1175/1520-0469(1988)045<2889:DATOAW>2.0.CO;2

Cai M, Kalnay E, Toth Z (2003) Bred vectors of the Zebiak–Cane Model and their potential application to ENSO predictions. J Clim 16:40–56. doi:10.1175/1520-0442(2003)016<0040:BVOTZC>2.0.CO;2

Chen D, Cane MA (2008) El Niño prediction and predictability. J Comput Phys 227:3625–3640. doi:10.1016/j.jcp.2007.05.014

Chen YQ, Battisti DS, Palmer RN, Barsugli J, Sarachik E (1997) A study of the predictability of tropical Pacific SST in a coupled atmosphere/ocean model using singular vector analysis. Mon Weather Rev 125:831–845. doi:10.1175/1520-0493(1997)125<0831:ASOTPO>2.0.CO;2

Chen D, Cane MA, Kaplan A, Zebiak SE, Huang D (2004) Predictability of El Niño over the past 148 years. Nature 428:733–736. doi:10.1038/nature02439

Fan Y, Allen MR, Anderson DLT, Balmaseda MA (2000) How predictability depends on the nature of uncertainty in initial conditions in a coupled model of ENSO. J Clim 13:3298–3313. doi:10.1175/1520-0442(2000)013<3298:HPDOTN>2.0.CO;2

Gebbie G, Eisenman I, Wittenberg A, Tziperman E (2007) Modulation of westerly wind bursts by sea surface temperature: a semistochastic feedback for ENSO. J Atmos Sci 64:3281–3295. doi:10.1175/JAS4029.1

Gill AE (1980) Some simple solutions for heat-induced tropical circulation. Q J R Meteorol Soc 106:447–462. doi:10.1002/qj.49710644905

Grinsted A, Moore JC, Jevrejeva S (2004) Application of the cross wavelet transform and wavelet coherence to geophysical time series. Nonlinear Process Geophys 11:561–566

Jin FF, Neelin JD, Ghil M (1994) El Niño on the devil's staircase: annual subharmonic steps to chaos. Science 264:70–72. doi:10.1126/science.264.5155.70

Jin EK, Kinter JLIII, Wang B, Park CK, Kang IS, Kirtman BP, Kug JS, Kumar A, Luo JJ, Schemm J, Shukla J, Yamagata T (2008) Current status of ENSO prediction skill in coupled ocean-atmosphere model. Clim Dyn 31:647–664. doi:10.1007/s00382-008-0397-3

Kirtman BP, Schopf PS (1998) Decadal variability in ENSO predictability and prediction. J Clim 11:2804–2822. doi:10.1175/1520-0442(1998)011<2804:DVIEPA>2.0.CO;2

Kirtman BP, Shukla J, Balmaseda M, Graham N, Penland C, Xue Y, Zebiak S (2002) Current status of ENSO forecast skill. A report to the Climate Variability and Predictability. (CLIVAR) Numerical Experimentation Group (NEG), CLIVAR Working Group on Seasonal to Interannual Prediction. Available online at http://www.clivar.org/publications/wg_reports/wgsip/nino3/report.htm

Kleeman R, Moore AM (1997) A theory for the limitation of ENSO predictability due to stochastic atmospheric transients. J Atmos Sci 54:753–767. doi:10.1175/1520-0469(1997)054<0753:ATFTLO>2.0.CO;2

Latif M, Anderson D, Barnett T, Cane M, Kleeman R, Leetma A, O'Brien J, Rosati A, Schneither E (1998) A review of the predictability and prediction of ENSO. J Geophys Res 103(C7):14375–14393. doi:10.1029/97JC03413

Li Z, Navon IM, Hussaini YM (2005) Analysis of the singular vectors of the full-physics FSU global spectral model. Tellus A Dyn Meterol Oceanogr 57:560–574. doi:10.1111/j.1600-0870.2005.00114.x

Lorenz EN (1965) A study of the predictability of a 28-variable atmospheric model. Tellus 17:321–333

Moore AM et al (2006) Optimal forcing patterns for coupled models of ENSO. J Clim 19:4683–4699. doi:10.1175/JCLI3870.1

Moore AM, Kleeman R (1996) The dynamics of error growth and predictability in a coupled model of ENSO. Q J R Meteorol Soc 122:1405–1446. doi:10.1002/qj.49712253409

Penland C, Sardeshmukh PD (1995) The optimal growth of tropical sea surface temperature anomalies. J Clim 8:1999–2024. doi:10.1175/1520-0442(1995)008<1999:TOGOTS>2.0.CO;2

Shukla J (1998) Predictability in the Midst of Chaos: a scientific basis for climate forecasting. Science 282:728–731. doi:10.1126/science.282.5389.728

Stern W, Miyakoda K (1995) Feasibility of seasonal forecasts inferred from multiple GCM simulations. J Clim 8:1071–1085. doi:10.1175/1520-0442(1995)008<1071:FOSFIF>2.0.CO;2

Suarez MJ, Schopf PS (1988) A delayed action oscillator for ENSO. J Atmos Sci 45:3283–3287. doi:10.1175/1520-0469(1988)045<3283:ADAOFE>2.0.CO;2

Tang Y, Deng Z (2009) Low-dimensional nonlinearity of ENSO and its impact on predictability. Physical D (submitted)

Tang Y, Hsieh WW (2003) ENSO simulation and predictions using a hybrid coupled model with data assimilation. J Jpn Meteor Soc 81(1):1–19. doi:10.2151/jmsj.81.1

Tang Y, Kleeman R, Miller S (2006) ENSO predictability of a fully coupled GCM model using singular vector analysis. J Clim 19:3361–3377. doi:10.1175/JCLI3771.1

Tang Y, Deng Z, Zhou X, Cheng Y, Chen D (2008) Interdecadal variation of ENSO predictability in multiple models. J Clim 21:4811–4833. doi:10.1175/2008JCLI2193.1

Vecchi GA, Harrison DE (2003) On the termination of the 2002–03 El Niño event. Geophys Res Lett 30:1946. doi:10.1029/2003GL017564

Vialard J, Vitart F, Balmaseda MA, Stockdale TN, Anderson DL (2005) An ensemble generation method for seasonal forecasting with an ocean-atmosphere coupled model. Mon Weather Rev 133:441–453. doi:10.1175/MWR-2863.1

Xue Y, Cane MA, Zebiak SE (1997a) Predictability of a coupled model of ENSO using singular vector analysis, Part I: optimal growth in seasonal background and ENSO cycles. Mon Weather Rev 125:2043–2056. doi:10.1175/1520-0493(1997)125<2043:POACMO>2.0.CO;2

Xue Y, Cane MA, Zebiak SE (1997b) Predictability of a coupled model of ENSO using singular vector analysis, part II: optimal growth and forecast skill. Mon Weather Rev 125:2057–2073. doi:10.1175/1520-0493(1997)125<2057:POACMO>2.0.CO;2

Zebiak SE, Cane MA (1987) A model El Niño-Southern oscillation. Mon Weather Rev 115:2262–2278. doi:10.1175/1520-0493(1987)115<2262:AMENO>2.0.CO;2

Zhou X, Tang Y, Deng Z (2007) The impact of nonlinear atmosphere on the fastest error growth of ENSO prediction. Clim Dyn 30:519–531. doi:10.1007/s00382-007-0302-5